# Near-field Localization with a Reconfigurable Intelligent Surface Acting as Lens

(article starts on next page)

# Near-field Localization with a Reconfigurable Intelligent Surface Acting as Lens

Zohair Abu-Shaban[*†], Kamran Keykhosravi[†], Musa Furkan Keskin[†],
George C. Alexandropoulos[‡], Gonzalo Seco-Granados[§], Henk Wymeersch[†]
[*]Cohda Wireless Pty Ltd., Australia,
[†]Department of Electrical Engineering, Chalmers University of Technology, Sweden
[‡]Department of Informatics and Telecommunications, National and Kapodistrian University of Athens, Greece
[§]Department of Telecommunications and Systems Engineering, Universitat Autonoma de Barcelona, Spain

*Abstract*—**Exploiting wavefront curvature enables localization with limited infrastructure and hardware complexity. With the introduction of reconfigurable intelligent surfaces (RISs), new opportunities arise, in particular when the RIS is functioning as a lens receiver. We investigate the localization of a transmitter using a RIS-based lens in close proximity to a single receive antenna element attached to reception radio frequency chain. We perform a Fisher information analysis, evaluate the impact of different lens configurations, and propose a two-stage localization algorithm. Our results indicate that positional beamforming can lead to better performance when *a priori* location information is available, while random beamforming is preferred when *a priori* information is lacking. Our simulation results for a moderate size lens operating at $28$ GHz showcased that decimeter-level accuracy can be attained within $3$ meters to the lens.**

## I. INTRODUCTION

Radio localization and sensing is gaining increased importance in fifth generation (5G) wireless communications systems enabling various commercial applications, such as personal navigation, indoor localization, radar sensing, and robot localization [1]. The combination of increased communication bandwidth and larger antenna arrays in 5G has led to improvements in localization accuracy, rendering efficient localization from a single base station possible [2]. This trend is continuing in beyond 5G research, where extremely large bandwidths at carrier frequencies up to 0.1 THz are being explored together with transceiver architectures based on extremely massive electromagnetically (EM) excited elements [3] (e.g., conventional dipoles and metamaterials), intended for combating path loss due to small element apertures. The latter factors enable a myriad of new opportunities for radio localization and sensing [4], [5].

Reconfigurable intelligent surfaces (RISs) [6], comprising large numbers of EM excited elements with dynamically tunable phase and/or amplitude, have been recently considered as a candidate technology for sixth generation (6G) wireless communication [1]. An RIS can operate as a smart reflector beyond Snell's law [7] or as a lens with nearly a continuous phase profile [8]–[10]. For the reflector operation mode, currently the most common via nearly passive hardware, RISs are deployed to enable high signal-to-noise ratios (SNRs) in the presence of obstructed line-of-sight. To achieve this

goal, sophisticated signal processing is used for both channel estimation and beamforming optimization [11]. On the other hand, RIS lenses can provide a good trade-off between hardware and signal processing complexity. Due to the usually large size of RISs, the corresponding channel models are distinct from standard multiple input multiple output (MIMO) models, as the following two common assumptions do not hold [12]: (*i*) constant signal power across the surface; and (*ii*) the presence of a planar wavefront. Hence, care must be taken when optimizing and evaluating the performance of communication and localization systems including RISs.

In the context of localization, RISs have been gaining attention in the past few years and an overview of the main challenges and opportunities for RIS reflectors can be found in [13]. The position (PEB) and orientation error bounds (OEB) of a MIMO setup were evaluated in [14], [15] which showed that an RIS can significantly enhance localization performance, provided that RIS phase profiles are designed appropriately. The problem was tackled in [16], which proposed a hierarchical RIS phase codebook. In [17], a RIS-aided multi-user localization protocol was proposed, based on signal strength measurements. In contrast, pure time-delay measurements were considered in [18], where RIS phase optimization and RIS selection were evaluated targeting PEB optimization. RIS reflectors have also been applied to sensing, e.g., for posture recognition [19]. RIS lens localization has been treated in [9], [20]–[22]. In [9], the localization Cramér-Rao bound for a continuous RIS was computed assuming curvature of the wavefront, revealing the impact of the RIS size, as well as RIS-induced impairments and the effect of different RIS deployments. RIS quantization effects on the localization performance were studied in [20]. In [22], the following three different architectures were compared: a RIS lens with a signal antenna, a non-reconfigurable lens with multiple antennas, and a standard planar array. The PEB was derived for all three cases, indicating that accurate localization is possible with a large RIS lens with low hardware complexity. There is also related work, such as [21], [23], on non-reconfigurable lens localization under the planar wavefront assumption, and on localization with curved wavefronts with MIMO radar [24], [25] with unknown transmit signal and fully digital arrays.
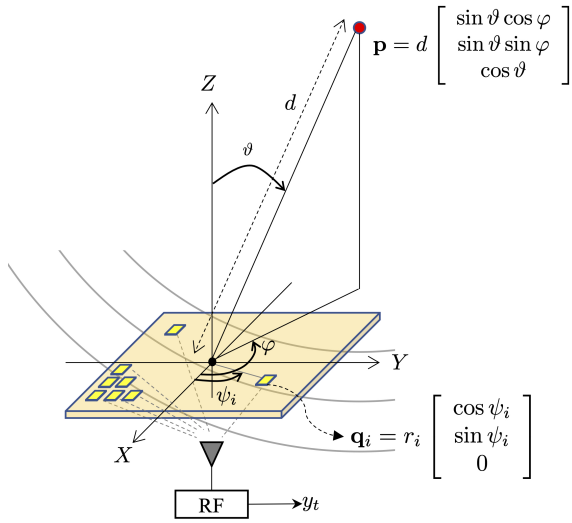
Fig. 1. The considered system setup with a single transmitting user and a single receiver comprising of RIS lens and a receive antenna element attached to a reception RF chain. We aim to localize the user in 3D based on the $T$ scalar baseband observations $y_t$, $\forall t = 1, 2, \ldots, T$.

In this paper, we study 3-dimensional (3D) localization using the low complexity RIS lens architecture of [22], which consists of reconfigurable discrete RIS lenses and a single antenna attached to a receive radio frequency (RF) chain. Our contributions are follows: (i) a Fisher information (FI) analysis with a closed form expression of the FI matrix (FIM), showing the dependence of the PEB on the RIS phase profiles; (ii) a low complexity location estimator whose performance is evaluated over a realistic channel model at 28 GHz.

*Notations:* Vectors are denoted in bold letters, whereas matrices in bold capital letters, $\boldsymbol{X}_{i:j,k:l}$ returns a matrix comprising rows $i$ through $j$ and columns $k$ through $l$ from $\boldsymbol{X}$. Operator $\circ$ is the point-wise product of vectors, $\mathbb{E}\{\cdot\}$ denotes expectation, $\cdot^\dagger$ the matrix pseudo-inverse, and $\jmath = \sqrt{-1}$. $\mathbf{1}_N$ and $\mathbf{0}_N$ represent the all-ones and all-zeros column vectors, respectively, of size $N$. The probability density function (pdf) of a random vector $\boldsymbol{x}$ is denoted by $p(\boldsymbol{x})$.

## II. SYSTEM AND CHANNEL MODELS

In this section, we describe the considered system setup for 3D localization with RIS lens and present the channel models that will be used for PEB analysis and performance evaluation.

### A. Geometry Model

We consider the wireless system setup of Fig. 1 including a single transmitting user at the location $\boldsymbol{p} = [x\ y\ z]^\top$ with $x, y \in \mathbb{R}$ and real-valued $z > 0$ and an $M$-element RIS lens laying in the XY plane with reference location $\mathbf{0}_3$, which is placed in close proximity to a single antenna with a respective receive RF chain, located at $\boldsymbol{p}_{\mathrm{ant}} \in \mathbb{R}^3$. Each $i$-th element of the RIS lens, with $i = 1, 2, \ldots, M$, is assumed to have the size $A = a \times a$ (typically, less or equal to $\lambda^2/4$ with $\lambda$ being the signal wavelength) and being located at $\boldsymbol{q}_i = [x_i\ y_i\ 0]^\top = r_i[\cos\psi_i\ \sin\psi_i\ 0]^\top \in \mathbb{R}^3$, where $r_i$ denotes the element's

distance from the origin and $\psi_i$ is the azimuth angle, as shown in Fig. 1. Let $\vartheta \in [0, \pi/2]$ be the angle between the Z axis (i.e., the normal of the RIS) and $\boldsymbol{p}$ and $\varphi \in [0, 2\pi]$ represent the angle between the projection of $\boldsymbol{p}$ on the XY plane and the X axis, measured counter-clockwise. We, henceforth, call $\vartheta, \varphi$ the angles-of-arrival (AoAs). Using the latter notations, we introduce the wavevector as a function of $\vartheta$ and $\varphi$:

$$\boldsymbol{k}(\vartheta, \varphi) = -\frac{2\pi}{\lambda} \begin{bmatrix} \sin\vartheta\cos\varphi \\ \sin\vartheta\sin\varphi \\ \cos\vartheta \end{bmatrix}, \tag{1}$$

which can be used in expressing the unknown position vector as $\boldsymbol{p} = -\lambda d\boldsymbol{k}(\vartheta, \varphi)/2\pi$, where $d$ is the Euclidean distance between $\boldsymbol{p}$ and the RIS reference location, i.e., $d \triangleq \|\boldsymbol{p}\|$. We model *a priori* information of the user location as a Gaussian pdf $p(\boldsymbol{p})$ having the mean $\boldsymbol{m}_p \in \mathbb{R}^3$ and covariance matrix represented by $\boldsymbol{\Sigma}_p \in \mathbb{R}^{3\times3}$.

### B. Signal Model

We assume a narrowband signal model according to which the transmitter sends the pilot signals $s_t$ with $\mathbb{E}\{|s_t|^2\} = E_s$ and $t = 1, 2, \ldots, T$ to the single-antenna receiver via the RIS lens for location estimation. The phase profile of the $M$ RIS lens elements at the time instant $t$ is represented by $\boldsymbol{\Omega}_t = \mathrm{diag}(\omega_{t,0}, \ldots, \omega_{t,M-1})$, where $|\omega_{t,i}| = 1\ \forall i = 0, 1, \ldots, M-1$. The baseband received signal at the output of the receive RF chain at each time $t$ can be mathematically expressed as

$$y_t = e^{\jmath\theta}\boldsymbol{h}_{\mathrm{ant}}^\top\boldsymbol{\Omega}_t(\boldsymbol{\rho}(\boldsymbol{p}) \circ \boldsymbol{a}(\boldsymbol{p}))s_t + n_t, \tag{2}$$

where $\theta = -\frac{2\pi d}{\lambda} + \theta_{\mathrm{sync}}$, in which $\theta_{\mathrm{sync}}$ is a global phase offset, which accounts for the lack of phase synchronization between transmitter and receiver and all other practical effects such as the phase response of the receive and transmit antennas, $\boldsymbol{h}_{\mathrm{ant}} \in \mathbb{C}^{M\times1}$ includes the fixed and known channel gains from the RIS lens to the single receive antenna, $\boldsymbol{\rho}(\boldsymbol{p}) \geq \mathbf{0}_M$ is the vector with the amplitudes of the wireless channels among the RIS elements and the transmitter, and $\boldsymbol{a}(\boldsymbol{p}) \in \mathbb{C}^{M\times1}$ is the vector of channel phases. Notation $n_t$ is the zero-mean additive Gaussian noise with variance $N_0/2$ per real dimension; we assume that $n_t$'s are independent and identically distributed. By introducing $\boldsymbol{w}_t = \boldsymbol{\Omega}_t\boldsymbol{h}_{\mathrm{ant}}$, $\boldsymbol{W} = [\boldsymbol{w}_1, \boldsymbol{w}_2, \ldots, \boldsymbol{w}_T] \in \mathbb{C}^{M\times T}$, $\boldsymbol{s} = [s_1, s_2, \ldots, s_T]^\top$, and $\boldsymbol{n} = [n_1, n_2, \ldots, n_T]^\top$, the measurement vector $\boldsymbol{y} = [y_1, y_2, \ldots, y_T]^\top$ can be compactly expressed as

$$\boldsymbol{y} = e^{\jmath\theta}\mathrm{diag}(\boldsymbol{s})\boldsymbol{W}^\top(\boldsymbol{\rho}(\boldsymbol{p}) \circ \boldsymbol{a}(\boldsymbol{p})) + \boldsymbol{n}. \tag{3}$$

For simplicity, we will next assume that $s_t = \sqrt{E_s}$, $\forall t$.

### C. Channel Model

Three channel models (CMs) for $\boldsymbol{h}_{\mathrm{ant}}$, $\boldsymbol{\rho}(\boldsymbol{p})$, and $\boldsymbol{a}(\boldsymbol{p})$ are henceforth considered using a common terminology in communication theory: the channel under the plane-wave model is termed as far-field, while under the curved wave model is termed near-field. We note that from an electromagnetic point

of view, both are far-field models[1]. Electromagnetic near-field effects within the Fraunhofer distance are ignored in this work. CM1 is the standard far-field model, where the amplitude of the received signal is constant across the RIS elements and the phase depends on AoAs. CM2 is the standard near-field model, where the amplitude is constant and the phase depends on the distance to each RIS element. Finally, CM3 is the improved near-field model from [12], where the amplitude at each RIS element depends on its location with respect to the user location, and the phase is as in CM2. The latter models for the involved channels are mathematically described as follows:

- *CM1 (standard far-field):* Under this model, it holds:

$$\boldsymbol{\rho}(\boldsymbol{p}) = \rho \mathbf{1}_M \qquad (4)$$

$$[\boldsymbol{a}(\boldsymbol{p})]_i = \exp(-\jmath \boldsymbol{q}_i^\top \boldsymbol{k}(\vartheta, \varphi)), \qquad (5)$$

where $\rho^2 = f(\vartheta, \varphi)\frac{A\cos\vartheta}{4\pi d^2}$ represents the common power for all RIS elements and $f(\vartheta, \varphi)$ is a correction factor (see later, in CM3).

- *CM2 (standard near-field):* Under this model, $\boldsymbol{\rho}(\boldsymbol{p}) = \rho \mathbf{1}_M$ as in CM1, but the phase accounts for wavefront curvature and is given by

$$[\boldsymbol{a}(\boldsymbol{p})]_i = \exp\left(-\jmath \frac{2\pi}{\lambda}\left(\|\boldsymbol{p} - \boldsymbol{q}_i\| - d\right)\right). \qquad (6)$$

It is readily verified that when $d \gg \|\boldsymbol{q}_i\|$, $\forall i$, then CM2 reverts to CM1.[2]

- *CM3 (improved near-field):* The amplitudes $\boldsymbol{\rho}(\boldsymbol{p})$ can be upper bounded according to [12, Lemma 1] as

$$[\boldsymbol{\rho}(\boldsymbol{p})]_i^2 = (12\pi)^{-1} \qquad (7)$$
$$\times \sum_{\substack{\mathsf{x}\in\mathcal{X}_i \\ \mathsf{y}\in\mathcal{Y}_i}} \frac{\mathsf{xy}}{(\mathsf{y}^2 + z^2)g(\mathsf{x},\mathsf{y})} + 2\arctan\left(\frac{\mathsf{xy}}{z^2 g(\mathsf{x},\mathsf{y})}\right),$$

in which $\mathcal{X}_i = \{a/2 + (x_i - x), a/2 - (x_i - x)\}$, $\mathcal{Y}_i = \{a/2 + (y_i - y), a/2 - (y_i - y)\}$, and $g(\mathsf{x},\mathsf{y}) = \sqrt{\mathsf{x}^2/z^2 + \mathsf{y}^2/z^2 + 1}$. In order to ensure consistency between the far-field and near-field models, we have found that $f(\vartheta, \varphi) = 1 - \sin^2(\vartheta)\sin^2(\varphi)$, which accounts for the specific linear polarization and the associated polarization loss considered in [12].[3] Then, for $d \gg \|\boldsymbol{q}_i\|$, $\forall i$, CM3 reverts to CM2, which in turn reverts to CM1.

These latter models are used throughout this paper, as follows. CM3 (the most realistic one) is used to generate $\boldsymbol{h}_{\mathrm{ant}}$, and also the actual unknown channel in the performance evaluation. In the Fisher information analysis, phase profile design, and algorithm derivation, simplified models CM1 and CM2 will be considered.

---

[1]As mentioned in [26], "the model used in the signal processing literature for near-field localization is in fact the far-field model of electromagnetics or an approximation thereof."

[2]To see this, note that $\|\boldsymbol{p}-\boldsymbol{q}_i\|-\|\boldsymbol{p}\| = d(1+r_i^2/d^2-2r_i/d\sin\vartheta\cos(\varphi-\psi_i))^{1/2}-d$, where $r_i$ and $\psi_i$ are defined in Fig. 1. For $d \gg r_i$, this becomes $-r_i\sin\vartheta\cos(\varphi-\psi_i)$, which does not depend on $d$.

[3]More specifically, the model in [12] assumes that the transmitter excites only the component of the electric field along the Y-axis (this is one of the two axis where the RIS lies). Note that this assumption cannot be valid for arbitrary user orientations, so the model should be generalized. This is beyond the scope of the current paper.

## III. FISHER INFORMATION ANALYSIS

### A. Introduction

The observations in baseband for the $T$ transmitted pilots at the receiver under CM2 can be expressed using (3) as

$$\boldsymbol{y} = \sqrt{E_s}\rho e^{\jmath\theta}\boldsymbol{W}^\top \boldsymbol{a}(\boldsymbol{p}) + \boldsymbol{n}. \qquad (8)$$

Introducing the noise-free observation $\boldsymbol{\mu} = \sqrt{E_s}\rho e^{\jmath\theta}\boldsymbol{W}^\top \boldsymbol{a}(\boldsymbol{p})$ and the $5 \times 1$ vector of unknowns $\boldsymbol{\eta} = [\rho\ \theta\ \boldsymbol{p}^\top]^\top$, the Fisher information matrix (FIM) $\boldsymbol{J}(\boldsymbol{\eta}) \in \mathbb{R}^{5\times 5}$ is defined as [27]

$$\boldsymbol{J}(\boldsymbol{\eta}) = \frac{2}{N_0}\Re\left\{\left(\frac{\partial\boldsymbol{\mu}}{\partial\boldsymbol{\eta}}\right)^{\mathrm{H}}\frac{\partial\boldsymbol{\mu}}{\partial\boldsymbol{\eta}}\right\}. \qquad (9)$$

Using the latter expression, the PEB in meters is given by

$$\mathrm{PEB} = \sqrt{\mathrm{trace}([\boldsymbol{J}^{-1}(\boldsymbol{\eta})]_{3:5,3:5})}, \qquad (10)$$

and can be related to the root mean squared error (RMSE) of any unbiased estimator $\hat{\boldsymbol{p}}$ by the inequality:

$$\mathrm{PEB} \leq \mathrm{RMSE} \triangleq \sqrt{\mathbb{E}\{\|\hat{\boldsymbol{p}} - \boldsymbol{p}\|^2\}}. \qquad (11)$$

### B. PEB Derivation

We can write the partial derivatives needed in (9) as $\partial\boldsymbol{\mu}/\partial\rho = \sqrt{E_s}e^{\jmath\theta}\boldsymbol{W}^\top\boldsymbol{a}(\boldsymbol{p})$, $\partial\boldsymbol{\mu}/\partial\theta = \sqrt{E_s}\rho e^{\jmath\theta}\boldsymbol{W}^\top\boldsymbol{a}(\boldsymbol{p})$, and $\partial\boldsymbol{\mu}/\partial\boldsymbol{p} = \sqrt{E_s}\rho e^{\jmath\theta}\boldsymbol{W}^\top\boldsymbol{D}(\boldsymbol{p})$, where $\boldsymbol{D}(\boldsymbol{p}) = \frac{\partial\boldsymbol{a}(\boldsymbol{p})}{\partial\boldsymbol{p}} \in \mathbb{C}^{M\times 3}$ which is computed as

$$\frac{\partial\boldsymbol{a}(\boldsymbol{p})}{\partial\boldsymbol{p}} = \jmath\frac{2\pi}{\lambda}\left(\mathrm{diag}(\boldsymbol{a}(\boldsymbol{p}))\boldsymbol{K}^\top + \boldsymbol{a}(\boldsymbol{p})\frac{\boldsymbol{p}^\top}{d}\right). \qquad (12)$$

In this expression, $\boldsymbol{K} = [\boldsymbol{e}_0, \boldsymbol{e}_1, \ldots, \boldsymbol{e}_{M-1}]$ with $\boldsymbol{e}_i = (\boldsymbol{q}_i - \boldsymbol{p})/\|\boldsymbol{q}_i - \boldsymbol{p}\|$. Introducing the positive semidefinite matrix $\boldsymbol{F} = \boldsymbol{W}^*\boldsymbol{W}^\top$, the non-zero entries of the FIM are given as follows. For its diagonal elements holds:

$$[\boldsymbol{J}(\boldsymbol{\eta})]_{1,1} = \frac{2E_s}{N_0}\boldsymbol{a}^{\mathrm{H}}(\boldsymbol{p})\boldsymbol{F}\boldsymbol{a}(\boldsymbol{p}), \qquad (13)$$

$$[\boldsymbol{J}(\boldsymbol{\eta})]_{2,2} = \frac{2E_s\rho^2}{N_0}\boldsymbol{a}^{\mathrm{H}}(\boldsymbol{p})\boldsymbol{F}\boldsymbol{a}(\boldsymbol{p}), \qquad (14)$$

$$[\boldsymbol{J}(\boldsymbol{\eta})]_{3:5,3:5} = \frac{2E_s\rho^2}{N_0}\Re\left(\boldsymbol{D}^{\mathrm{H}}(\boldsymbol{p})\boldsymbol{F}\boldsymbol{D}(\boldsymbol{p})\right), \qquad (15)$$

and for the off-diagonal elements (above the main diagonal):

$$[\boldsymbol{J}(\boldsymbol{\eta})]_{1:2,3:5} = \frac{2E_s\rho}{N_0}\left[\begin{array}{c}\Re\left(\boldsymbol{a}^{\mathrm{H}}(\boldsymbol{p})\boldsymbol{F}\boldsymbol{D}(\boldsymbol{p})\right) \\ \rho\Im\left(\boldsymbol{a}^{\mathrm{H}}(\boldsymbol{p})\boldsymbol{F}\boldsymbol{D}(\boldsymbol{p})\right)\end{array}\right]. \qquad (16)$$

To obtain further insights on the PEB performance, we derive the equivalent FIM of the user location as [28]

$$\boldsymbol{J}(\boldsymbol{p}) = [\boldsymbol{J}(\boldsymbol{\eta})]_{3:5,3:5} \qquad (17)$$
$$- [\boldsymbol{J}(\boldsymbol{\eta})]_{3:5,1:2}[\boldsymbol{J}(\boldsymbol{\eta})]_{1:2,1:2}^{-1}[\boldsymbol{J}(\boldsymbol{\eta})]_{1:2,3:5}$$
$$= \frac{2\rho^2 E_s}{N_0}\Re\left\{\boldsymbol{D}^{\mathrm{H}}(\boldsymbol{p})\left[\boldsymbol{F} - \frac{\boldsymbol{F}\boldsymbol{a}(\boldsymbol{p})\boldsymbol{a}^{\mathrm{H}}(\boldsymbol{p})\boldsymbol{F}}{\boldsymbol{a}^{\mathrm{H}}(\boldsymbol{p})\boldsymbol{F}\boldsymbol{a}(\boldsymbol{p})}\right]\boldsymbol{D}(\boldsymbol{p})\right\}.$$

By defining $\boldsymbol{E} = \boldsymbol{W}^\top\boldsymbol{D}(\boldsymbol{p})$ and $\boldsymbol{c} = \boldsymbol{W}^\top\boldsymbol{a}(\boldsymbol{p})$, we obtain

$$\boldsymbol{J}(\boldsymbol{p}) = \frac{2\rho^2 E_s}{N_0}\Re\left\{\boldsymbol{E}^{\mathrm{H}}\left(\boldsymbol{I} - \frac{\boldsymbol{c}\boldsymbol{c}^{\mathrm{H}}}{\|\boldsymbol{c}\|^2}\right)\boldsymbol{E}\right\} \qquad (18)$$
$$= \frac{2\rho^2 E_s}{N_0}\Re\left\{\boldsymbol{E}^{\mathrm{H}}\boldsymbol{\Pi}_{\boldsymbol{c}}^\perp\boldsymbol{E}\right\} = \frac{2\rho^2 E_s}{N_0}\Re\left\{(\boldsymbol{\Pi}_{\boldsymbol{c}}^\perp\boldsymbol{E})^{\mathrm{H}}\boldsymbol{\Pi}_{\boldsymbol{c}}^\perp\boldsymbol{E}\right\},$$

where $\boldsymbol{\Pi}_{\boldsymbol{c}}^{\perp}\boldsymbol{E}$ represents the component of $\boldsymbol{W}^{\top}\boldsymbol{D}(\boldsymbol{p})$ that lies in the subspace orthogonal to $\boldsymbol{c} = \boldsymbol{W}^{\top}\boldsymbol{a}(\boldsymbol{p})$; $\boldsymbol{\Pi}_{\boldsymbol{c}}^{\perp}$ is the orthogonal projection operator over $\boldsymbol{c}$. Thus, the PEB can be expressed in a compact form up to an SNR scaling factor as $\text{PEB} = \sqrt{\text{trace}(\Re\{\boldsymbol{E}^{\mathrm{H}}\boldsymbol{\Pi}_{\boldsymbol{c}}^{\perp}\boldsymbol{E}\}^{-1})}$. Obviously, if the derivative $\boldsymbol{D}(\boldsymbol{p})$ is almost orthogonal to $\boldsymbol{a}(\boldsymbol{p})$ (after projection through $\boldsymbol{W}^{\top}$), then a large amount of positional information is available resulting in small PEB. In other words, the position estimation accuracy depends on how well the RIS phase profile can distinguish the steering vector and its derivative. In addition, when $d \gg r_i$ (i.e., under the plane wave model), it holds $\text{diag}(\boldsymbol{a}(\boldsymbol{p}))\boldsymbol{K}^{\top} \to -\boldsymbol{a}(\boldsymbol{p})\boldsymbol{p}^{\top}/d$, and thus $\boldsymbol{J}(\boldsymbol{p}) \to 0$. This indicates that the PEB increases further away from the RIS-based lens, irrespective of the path loss.

## IV. RIS PHASE PROFILE DESIGN

The performance of the location estimation depends on the choice of RIS phase profiles $\boldsymbol{\Omega}_t$. In order to remove the effect of the phases in $\boldsymbol{h}_{\text{ant}}$, we set $\boldsymbol{\Omega}_t = \boldsymbol{\Omega}_{\text{ant}}\tilde{\boldsymbol{\Omega}}_t$, where the fixed phases $\boldsymbol{\Omega}_{\text{ant}} = \text{diag}(\omega_{\text{ant},0}, \ldots, \omega_{\text{ant},M-1})$ ensure that $[\boldsymbol{h}_{\text{ant}}^{\top}\boldsymbol{\Omega}_{\text{ant}}]_i = |[\boldsymbol{h}_{\text{ant}}^{\top}]_i|, \forall i$ [22], exploiting the knowledge of $\boldsymbol{h}_{\text{ant}}$. It then remains to design $\tilde{\boldsymbol{\Omega}}_t = \text{diag}(\tilde{\omega}_{t,0}, \ldots, \tilde{\omega}_{t,M-1})$. We consider the following three designs for $\tilde{\omega}_{t,i} \ \forall i,t$:

- *Random:* In this approach, we set $\tilde{\omega}_{t,i} = \exp(\jmath\psi_{t,i})$, where $\psi_{t,i} \sim \mathcal{U}(0, 2\pi)$ independently for each $i$-th RIS element and each time instant $t$.
- *Directional:* We set each phase configuration under CM1 as $\tilde{\omega}_{t,i} = \exp(+\jmath\boldsymbol{q}_i^{\top}\boldsymbol{k}(\vartheta^{(k)}, \varphi^{(k)}))$, where the samples $\vartheta^{(k)}$ and $\varphi^{(k)}$ are obtained from the *a priori* pdf $p(\boldsymbol{p})$.
- *Positional:* Under CM2, we set $\tilde{\omega}_{t,i} = \exp\left(+\jmath\frac{2\pi}{\lambda}\left(\|\boldsymbol{p}^{(k)} - \boldsymbol{q}_i\| - d^{(k)}\right)\right)$, where $\boldsymbol{p}^{(k)}$ and $d^{(k)}$ are sampled from $p(\boldsymbol{p})$.

To understand the difference between the different phase profiles, we show the SNR as a function of the location in the plane $Y = X$ for a single realization of a phase profile for each of the three choices. The SNR is defined as

$$\text{SNR} = \frac{1}{T}\sum_{t=1}^{T}\frac{E_s\rho^2}{N_0}|\boldsymbol{w}_t^{\top}\boldsymbol{a}(\boldsymbol{p})|^2. \tag{19}$$

The results are shown in Fig. 2, assuming an *a priori* position distribution with mean $[0.1\,0.1\,0.1]^{\top}$ and covariance $0.01\boldsymbol{I}_3$. We observe that the random case leads to uniform SNR for all locations subject to path loss, with reduced values close to the end-fire of the RIS. For the directional case, a higher SNR is achieved along the chosen direction, with reduced SNR in other locations, as compared to the random case. Finally, for the positional case, beams tend to be slightly broader.

## V. LOCATION ESTIMATION

### A. Maximum Likelihood Estimator

We introduce $\alpha = \rho e^{j\theta}$ so that the maximum likelihood estimate of the channel gain and user location is given by

$$[\hat{\alpha}, \hat{\boldsymbol{p}}] = \arg\max_{\alpha,\boldsymbol{p}} f(\boldsymbol{y}|\alpha, \boldsymbol{p}) \tag{20}$$

$$= \arg\min_{\alpha,\boldsymbol{p}} \|\boldsymbol{y} - \sqrt{E_s}\alpha\boldsymbol{W}^{\top}\boldsymbol{a}(\boldsymbol{p})\|^2. \tag{21}$$

Solving for $\alpha$, yields the gain estimation as a function of $\boldsymbol{p}$:

$$\hat{\alpha}(\boldsymbol{p}) = \frac{\boldsymbol{a}^{\mathrm{H}}(\boldsymbol{p})\boldsymbol{W}^*\boldsymbol{y}}{\sqrt{E_s}\|\boldsymbol{W}^{\top}\boldsymbol{a}(\boldsymbol{p})\|^2}. \tag{22}$$

Consequently, the estimate $\boldsymbol{p}$ can be calculated as:

$$\hat{\boldsymbol{p}} = \arg\min_{\boldsymbol{p}} \|\boldsymbol{y} - \sqrt{E_s}\hat{\alpha}(\boldsymbol{p})\boldsymbol{W}^{\top}\boldsymbol{a}(\boldsymbol{p})\|^2. \tag{23}$$

$$= \arg\min_{\boldsymbol{p}} \|\boldsymbol{\Pi}_{\boldsymbol{c}}^{\perp}\boldsymbol{y}\|^2, \tag{24}$$

where $\boldsymbol{\Pi}_{\boldsymbol{c}}^{\perp}$ is the orthogonal projection operator over $\boldsymbol{c} = \boldsymbol{W}^{\top}\boldsymbol{a}(\boldsymbol{p})$, as defined in (18).

### B. Low Complexity Localization

To solve (23), we make use of the underlying structure of the optimization problem in spherical coordinates, which leads to a three-stage estimator, as follows. We first express each $i$-th exponential term in (5) as

$$[\boldsymbol{a}(\vartheta, \varphi)]_i = \exp\left(-\jmath\frac{2\pi}{\lambda}r_i\sin(\vartheta)\cos(\varphi - \psi_i)\right). \tag{25}$$

Similar to [29], we employ the Jacobi-Anger expansion to re-express (25) as

$$[\boldsymbol{a}(\vartheta, \varphi)]_i = \sum_{n=-\infty}^{\infty}\jmath^n J_n\left(-\frac{2\pi}{\lambda}r_i\sin(\vartheta)\right)e^{\jmath n(\varphi - \psi_i)}, \tag{26}$$

where $J_n(\cdot)$ is the $n$-th order Bessel function of the first kind. Neglecting the terms with $|n| > N$ for a given $N$ (note that $|J_n(\cdot)|$ decays to zero as $|n|$ increases), we obtain

$$[\boldsymbol{a}(\vartheta, \varphi)]_i \approx \sum_{n=-N}^{N}\jmath^n J_n\left(-\frac{2\pi}{\lambda}r_i\sin(\vartheta)\right)e^{\jmath n(\varphi - \psi_i)}. \tag{27}$$

By defining the following parameters for $n = -N, \ldots, N$:

$$[\boldsymbol{g}_i(\vartheta)]_n = \jmath^n J_n\left(-\frac{2\pi}{\lambda}r_i\sin(\vartheta)\right)e^{-\jmath n\psi_i} \tag{28}$$

$$[\boldsymbol{h}(\varphi)]_n = e^{\jmath n\varphi}, \tag{29}$$

yields $[\boldsymbol{a}(\vartheta, \varphi)]_i = \boldsymbol{g}_i^{\top}(\vartheta)\boldsymbol{h}(\varphi)$. It can be easily verified that $\boldsymbol{a}(\vartheta, \varphi) \approx \boldsymbol{G}^{\top}(\vartheta)\boldsymbol{h}(\varphi)$, where $\boldsymbol{G}(\vartheta) = [\boldsymbol{g}_0(\vartheta) \ \ldots \ \boldsymbol{g}_{M-1}(\vartheta)]$. Now, the angular steering vector $\boldsymbol{a}(\vartheta, \varphi)$ has a form that is separable in the angles $\vartheta$ and $\varphi$.

We are now ready to proceed with our three-stage estimator.

1) *Estimation of $\vartheta$:* Under CM1, we rewrite $\boldsymbol{y}$ in (8) as

$$\boldsymbol{y} = \sqrt{E_s}\alpha\boldsymbol{W}^{\top}\boldsymbol{G}^{\top}(\vartheta)\boldsymbol{h}(\varphi) + \boldsymbol{n}. \tag{30}$$

By introducing the unstructured vector $\boldsymbol{v} = \sqrt{E_s}\alpha\boldsymbol{h}(\varphi)$, the estimate of $\boldsymbol{v}$ can be expressed by the following function of $\vartheta$: $\hat{\boldsymbol{v}}(\vartheta) = \left(\boldsymbol{G}^*(\vartheta)\boldsymbol{W}^*\right)^{\dagger}\boldsymbol{G}^*(\vartheta)\boldsymbol{W}^*\boldsymbol{y}$. Hence, the estimation for angle $\vartheta$ can be obtained as

$$\hat{\vartheta} = \arg\min_{\vartheta} \|\boldsymbol{y} - \boldsymbol{W}^{\top}\boldsymbol{G}^{\top}(\vartheta)\hat{\boldsymbol{v}}(\vartheta)\|^2, \tag{31}$$

which can be solved with a simple line search.

2) *Estimation of $\varphi$:* Again, under CM1 and using the estimate $\hat{\vartheta}$, expression (30) can be written as $\boldsymbol{y} = \sqrt{E_s}\alpha\boldsymbol{W}^{\top}\boldsymbol{G}^{\top}(\hat{\vartheta})\boldsymbol{h}(\varphi) + \boldsymbol{n}$. We estimate $\alpha$ for each
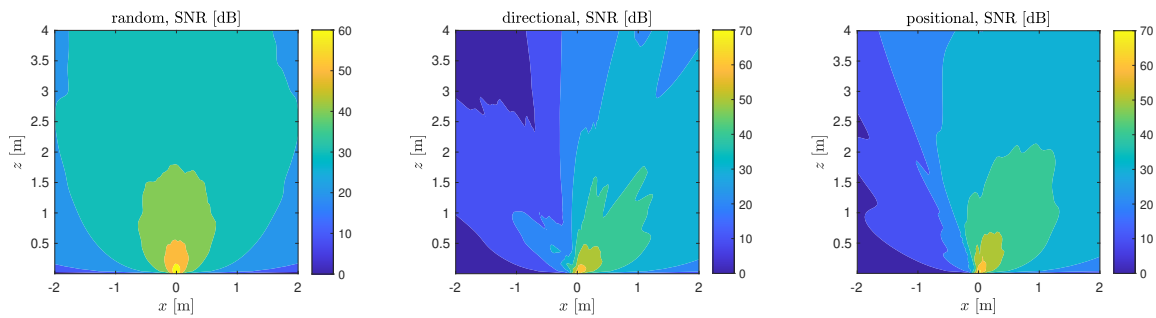
Fig. 2. SNR from (19) in dB in the $X = Y$ plane for random, directional, and positional RIS phase profiles, with $\boldsymbol{m}_p = [0.1\,0.1\,0.1]^\top$ and $\boldsymbol{\Sigma}_p = 0.01\boldsymbol{I}_3$. For visualization purposes, the SNR values are truncated at 0 dB. Infinite resolution of the phase profiles is assumed, though with 2 or 3 bits, the SNR is close to the results in the figure.

value of $\varphi$ similarly as in (22), but replacing $\boldsymbol{a}(\boldsymbol{p})$ with $\boldsymbol{G}^\top(\hat{\vartheta})\boldsymbol{h}(\varphi)$, leading to $\hat{\alpha}(\varphi)$. Then, we can solve for angle $\varphi$ as follows:

$$\hat{\varphi} = \arg\min_{\varphi} \|\boldsymbol{y} - \sqrt{E_s}\hat{\alpha}(\varphi)\boldsymbol{W}^\top\boldsymbol{G}^\top(\hat{\vartheta})\boldsymbol{h}(\varphi)\|^2, \quad (32)$$

which requires a second line search.

3) *Estimation of $d$:* Under CM2, given the estimates $\hat{\vartheta}$ and $\hat{\varphi}$, we introduce $\boldsymbol{p}(d) = d[\sin\hat{\vartheta}\cos\hat{\varphi}\ \sin\hat{\vartheta}\sin\hat{\varphi}\ \cos\hat{\vartheta}]^\top$, from which we determine $\hat{\alpha}(\boldsymbol{p}(d))$, an unstructured estimate of $\alpha$ as in (22), and finally solve the optimization:

$$\hat{d} = \arg\min_{d} \|\boldsymbol{y} - \sqrt{E_s}\hat{\alpha}(\boldsymbol{p}(d))\boldsymbol{W}^\top\boldsymbol{a}(\boldsymbol{p}(d))\|^2, \quad (33)$$

which requires a third and final line search.

## VI. NUMERICAL RESULTS

### A. Simulation Setup

We consider a RIS with $M = 2500$ elements (i.e., $50 \times 50$) at 28 GHz with $\lambda/2$ spacing and area $A = \lambda^2/4$. The single receive antenna is placed behind the RIS lens at $[0\ 0\ -\lambda]^\top$. The transmit power is 1 mW, the noise power spectral density is set to $-174$ dBm/Hz and the reception noise figure to 8 dB. We set the number of time instants to $T = 200$ and the bandwidth to 1 MHz, so that localization is based on a 0.2 ms observation. We consider a user with wavevector $\boldsymbol{k}$ along the direction $[1\ 1\ 1]^\top$. The channels $\boldsymbol{h}_{\text{ant}}$ and $\boldsymbol{\rho}(\boldsymbol{p}) \circ \boldsymbol{a}(\boldsymbol{p})$ in (3) are generated according to CM3, as defined in (6) and (7). A priori information of the user location is of the form of a Gaussian pdf $p(\boldsymbol{p}) = \mathcal{N}(\boldsymbol{p}; \boldsymbol{m}_p, \boldsymbol{\Sigma}_p)$ with $\boldsymbol{\Sigma}_p = \sigma^2\boldsymbol{I}_3$. This a priori information is only used to design the RIS phase profiles, not during localization nor in the PEB calculation. The three RIS profiles designs from Section IV will be evaluated for $\sigma \in \{0.1, 1\}$ m. The channel estimator uses $N = 5$ in the expansion (27).

### B. PEB Evaluation

The PEB as a function of distance in meters is illustrated in Fig. 3 for the three selected RIS phase profile designs and different values of $\sigma$. As a reference, the PEB corresponding to the prior is shown as a horizontal line. We observe that, even with the simple randomized phase profile, relatively low PEB values can be attained, below 1 m for user location distances up to 10 m from the RIS lens. With directional or

positional phase profiles, the PEB can be substantially reduced. The positional phase profile performs slightly better than the directional phase profile, but the difference is negligible. Better a priori information (i.e., smaller $\sigma$) leads to better PEB. Note that for $\sigma = 0.1$ m, the PEB due to the RIS measurements is only better than the a priori PEB below 10 m.

### C. Localization Accuracy

In Fig. 4, we show the RMSE of the proposed three-stage localization algorithm, as a function of distance in meters to the RIS. Since we use a finite resolution in the angle and delay domain searches (360 bins for $\varphi$, 90 for $\vartheta$ and 500 for $d$), combined with the fact that the CM1 model assumed in the first two stages of the algorithm does not hold for small distances, we are unable to attain the PEB in that regime. With this in mind, the performance of the randomized codebook is close to the PEB, leading to sub-meter localization RMSE within 10 meters from the RIS lens. Paradoxically, the performance under the directional RIS phase profile (shown only for $\sigma = 0.1$ m) is far worse than predicted by the bounds. This can be explained as follows: the directional phase profiles focus energy in the direction of the user, which leads to $\|\boldsymbol{W}^\top\boldsymbol{a}(\boldsymbol{p})\|^2 \approx 0$ for most locations $\boldsymbol{p}$ different from the true location. Hence, the objective function (23) is nearly flat everywhere, with very narrow peaks around the true position. Due to the finite resolution of the proposed estimators, we miss this peak with high probability, leading to outliers and a degraded RMSE.

## VII. CONCLUSIONS

We considered the problem of localizing a transmitter in 3D using a RIS-based lens and a single receive antenna with a respective RF chain. By exploiting the wavefront curvature, the user location can be estimated, provided that several RIS phase configurations are used. A Fisher information analysis provides insight into the design of these phase configurations. We have also presented a low-complexity 3D localization algorithm, which transforms the 3D problem into 3 one-dimensional problems. Simulation results confirm the validity of the approach and highlight that RIS configurations optimized for localization performance may suffer from degraded performance when not complemented with high-resolution
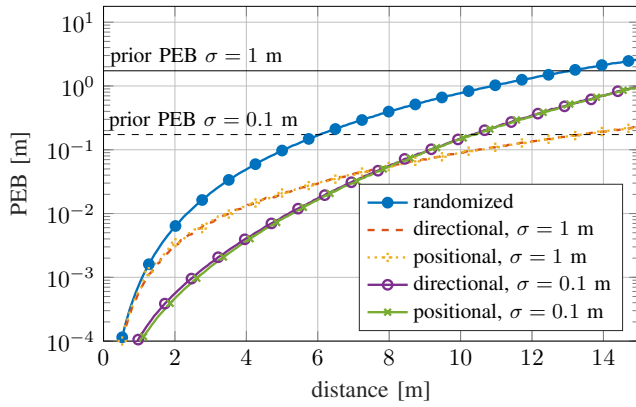
Fig. 3. PEB as a function of distance to the RIS lens.
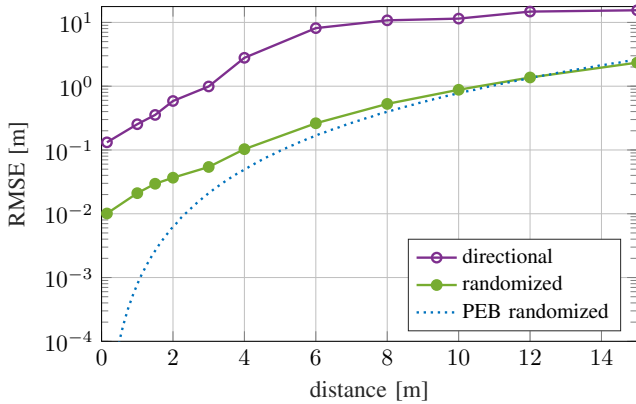


Fig. 4. RMSE as a function of distance to the RIS lens.

estimators. Based on this, we recommend random RIS phase configurations when low complexity estimation is targeted. There are several avenues for further research, including using the amplitude of the received signal for localization, and the inclusion of multi-path and multi-user localization.

### REFERENCES

[1] R. Keating, M. Säily, J. Hulkkonen, and J. Karjalainen, "Overview of positioning in 5G new radio," in *Proc. IEEE ISWCS*, Oulu, Finland, Aug. 2019.

[2] A. Shahmansoori, G. E. Garcia, G. Destino, G. Seco-Granados, and H. Wymeersch, "Position and orientation estimation through millimeter-wave MIMO in 5G systems," *IEEE Trans. Wireless Commun.*, vol. 17, no. 3, pp. 1822–1835, Mar. 2018.

[3] "The next hyper-connected experience for all," White Paper, Samsung 6G Vision, Jun. 2020.

[4] G. C. Alexandropoulos, R. Khayatzadeh, M. Kamoun, Y. Ganghua, and M. Debbah, "Indoor time reversal wireless communication: Experimental results for localization and signal coverage," in *Proc. IEEE ICASSP*, Brighton, UK, May 2019.

[5] A. Bourdoux, A. N. Barreto, B. van Liempd, C. de Lima, D. Dardari *et al.*, "6G white paper on localization and sensing," *IEEE Access*, 2021.

[6] C. Huang, A. Zappone, G. C. Alexandropoulos, M. Debbah, and C. Yuen, "Reconfigurable intelligent surfaces for energy efficiency in wireless communication," *IEEE Trans. Wireless Commun.*, vol. 18, no. 8, pp. 4157–4170, Aug. 2019.

[7] M. Di Renzo, M. Debbah, D.-T. Phan-Huy, A. Zappone, M.-S. Alouini *et al.*, "Smart radio environments empowered by reconfigurable AI meta-surfaces: An idea whose time has come," *EURASIP J. Wireless Commun. Netw.*, vol. 2019, no. 1, pp. 1–20, May 2019.

[8] Y. Zeng, R. Zhang, and Z. N. Chen, "Electromagnetic lens-focusing antenna enabled massive MIMO: Performance improvement and cost reduction," *IEEE J. Sel. Areas Commun.*, vol. 32, no. 6, pp. 1194–1206, Jun. 2014.

[9] S. Hu, F. Rusek, and O. Edfors, "Beyond massive MIMO: The potential of positioning with large intelligent surfaces," *IEEE Trans. Signal Process.*, vol. 66, no. 7, pp. 1761–1774, Apr. 2018.

[10] C. Huang, S. Hu, G. C. Alexandropoulos, A. Zappone, C. Yuen *et al.*, "Holographic MIMO surfaces for 6G wireless networks: Opportunities, challenges, and trends," *IEEE Wireless Commun.*, to appear, 2020.

[11] B. Zheng and R. Zhang, "Intelligent reflecting surface-enhanced OFDM: Channel estimation and reflection optimization," *IEEE Wireless Commun. Lett.*, vol. 9, no. 4, pp. 518–522, Apr. 2020.

[12] E. Björnson and L. Sanguinetti, "Power scaling laws and near-field behaviors of massive MIMO and intelligent reflecting surfaces," *IEEE Open Journal of the Communications Society*, vol. 1, pp. 1306–1324, 2020.

[13] H. Wymeersch, J. He, B. Denis, A. Clemente, and M. Juntti, "Radio localization and mapping with reconfigurable intelligent surfaces: Challenges, opportunities, and research directions," *IEEE Vehicular Technology Magazine*, vol. 15, no. 4, pp. 52–61, 2020.

[14] A. Elzanaty, A. Guerra, F. Guidi, and M.-S. Alouini, "Reconfigurable intelligent surfaces for localization: Position and orientation error bounds," *arXiv preprint arXiv:2009.02818*, 2020.

[15] J. He, H. Wymeersch, L. Kong, O. Silvén, and M. Juntti, "Large intelligent surface for positioning in millimeter wave MIMO systems," in *Proc. IEEE VTC-Spring*, Antwerp, Belgium, May 2020.

[16] J. He, H. Wymeersch, T. Sanguanpuak, O. Silvén, and M. Juntti, "Adaptive beamforming design for mmwave RIS-aided joint localization and communication," in *Proc. IEEE WCNC*, Seoul, Korea, Apr. 2020.

[17] H. Zhang, J. Hu, H. Zhang, B. Di, K. Bian *et al.*, "Metaradar: Indoor localization by reconfigurable metamaterials," *IEEE Transactions on Mobile Computing*, 2020.

[18] H. Wymeersch and B. Denis, "Beyond 5G wireless localization with reconfigurable intelligent surfaces," in *Proc. IEEE ICC*, Dublin, Ireland, Jun. 2020.

[19] J. Hu, H. Zhang, B. Di, L. Li, K. Bian *et al.*, "Reconfigurable intelligent surface based RF sensing: Design, optimization, and implementation," *IEEE J. Sel. Areas Commun.*, vol. 38, no. 11, pp. 2700–2716, 2020.

[20] J. V. Alegría and F. Rusek, "Cramér-rao lower bounds for positioning with large intelligent surfaces using quantized amplitude and phase," in *Proc. IEEE Asilomar CSSC*, Pasific Grove, USA, Nov. 2019, pp. 10–14.

[21] J. Yang, S. Jin, Y. Han, M. Matthaiou, and Y. Zhu, "3-D position and velocity estimation in 5G mmWave CRAN with lens antenna arrays," in *Proc. IEEE VTC-Fall*, Honolulu, USA, Sep. 2019.

[22] F. Guidi and D. Dardari, "Radio positioning with EM processing of the spherical wavefront," *arXiv preprint arXiv:1912.13331*, 2019.

[23] S. A. Shaikh and A. M. Tonello, "Radio source localization in multipath channels using EM lens assisted massive antennas arrays," *IEEE Access*, vol. 7, pp. 9001–9012, Jan. 2019.

[24] H. Godrich, A. M. Haimovich, and R. S. Blum, "Target localization accuracy gain in mimo radar-based systems," *IEEE Trans. Inf. Theory*, vol. 56, no. 6, pp. 2783–2803, Jun. 2010.

[25] W. Zuo, J. Xin, H. Ohmori, N. Zheng, and A. Sano, "Subspace-based algorithms for localization and tracking of multiple near-field sources," *IEEE J. Sel. Topics Signal Process.*, vol. 13, no. 1, pp. 156–171, Mar. 2019.

[26] B. Friedlander, "Localization of signals in the near-field of an antenna array," *IEEE Trans. Signal Process.*, vol. 67, no. 15, pp. 3885–3893, Aug. 2019.

[27] H. L. V. Trees, *Detection, Estimation, and Modulation Theory*. John Wiley & Sons, New York, 2004.

[28] Y. Shen and M. Z. Win, "Fundamental limits of wideband localization—Part I: A general framework," *IEEE Trans. Inf. Theory*, vol. 56, no. 10, pp. 4956–4980, Oct. 2010.

[29] Y. Wang, Y. Zhang, Z. Tian, G. Leus, and G. Zhang, "Super-resolution channel estimation for arbitrary arrays in hybrid millimeter-wave massive MIMO systems," *IEEE J. Sel, Topics Signal Process.*, vol. 13, no. 5, pp. 947–960, Sep. 2019.